Surface & Coatings Technology 416 (2021) 127155

Contents lists available at ScienceDirect

Surface & Coatings Technology

journal homepage: www.elsevier.com/locate/surfcoat

Characterization of single- and multilayer cold-spray coating of Zn on AZ31B

Bahareh Marzbanrad, Ehsan Toyserkani, Hamid Jahed *

Mechanical and Mechatronics Engineering Department, University of Waterloo, Canada

ARTICLE INFO

Keywords:
Cold spray
Multi-material deposition
Residual stress
Magnesium
Zinc
Aluminum

ABSTRACT

Zinc, a soft material with a low melting point and high corrosion resistance, was coated onto AZ31B Mg alloy using different cold spraying process parameters. The physical and mechanical properties of the resulting Zn/AZ31B samples were then investigated to explore the effect of the process parameters on the microstructural and mechanical characteristics. The results obtained via X-ray diffraction show the formation of an intermetallic material at the interface of Zn/AZ31B even at low process temperatures. In addition, spherical droplets of Zn were observed at the surface, confirming the partial melting of Zn particles during the impact. This partial melting is believed to lead to the formation of intermetallic compounds during solidification. To engineer the residual stress induced in the cold spraying process, a thin layer of dense Zn was then used as an intermediate layer before coating with Al7075, forming a multilayered surface of Al7075/Zn/AZ31B. Because of the higher thermal expansion coefficient of Zn compared with those of Al7075 and AZ31B, beneficial compressive residual stress could be created in all three layers of this novel multilayer deposition. Without the Zn interlayer, Al7075/AZ31B under the same coating parameters exhibited undesirable tensile residual stress in the substrate.

1. Introduction

Cold gas dynamic spraying is a solid-state material-deposition technology with applications in surface modification, repair, and 3D printing structures. Unlike thermal spraying or fusion-based additive manufacturing, cold spraying uses kinetic energy to print/coat high- and low-melting temperature powders. A convergent–divergent de Laval nozzle supersonically accelerates micron-sized particles through a pressurized gas with relatively low temperature. The high-velocity particles impact a substrate with high kinetic energy, consequently experiencing intense deformation [1]. This intensive plastic deformation of particles and the significant amount of localized heat upon impact result in mechanical and metallurgical bonding with the substrate [2]. A byproduct of cold-spray deposition is residual stress. These stresses have been shown to result from a peening effect caused by the supersonic impact and thermally activated stresses due to heat transfer during the process [3,4]. Although cold spraying operates at temperatures lower than the melting temperature, the heat generated by the impact and the heat input through the carrier gas increase the temperature of the coated samples [5]. The interaction of induced temperature and particle impact may lead to stress relief, particularly in temperature-sensitive materials [3,6]. In this case, the thermal expansion coefficient (CTE) of the powder and substrate plays a significant role in developing the residual thermal strains when the coated sample temperature drops from that of coating to room temperature (20–23 °C). Further, bombarding the substrate with high-velocity particles creates a peening-like, impact-induced compressive residual stress. However, the thermal expansion mismatch between the coating and substrate can partially or entirely neutralize the peening compressive stress [3,5,7]. This phenomenon is more profound for temperature-sensitive materials such as Mg. For instance, when Al7075 powder was coated on Mg alloy structures, the thermal mismatch affected the impact-induced compressive residual stress, transforming it into tensile residual stress [3,8]. To address these issues, the use of an intermediate layer of a material with a CTE greater than those of Al and Mg can serve as a practical approach in controlling the detrimental effects of thermal mismatch.

Zn, as a corrosion-resistant metal, is widely used to chemically protect ferrous and Mg alloys from corrosion and surface degradation [9]. Moreover, as a biodegradable material, Zn has been considered for medical applications owing to its corrosion resistance and compatibility with the human body [10,11]. Furthermore, Zn, with its hexagonal close-packed structure, has a few slip systems, resulting in low plasticity

* Corresponding author.
E-mail address: hamid.jahed@uwaterloo.ca (H. Jahed).

https://doi.org/10.1016/j.surfcoat.2021.127155
Received 11 January 2021; Received in revised form 1 April 2021; Accepted 3 April 2021
Available online 9 April 2021

and deformability. However, the low mechanical strength and low melting temperature of this soft material provide good ductility and a low critical velocity, making it a desirable material for cold-spray coatings. To date, only a few studies have explored cold-spray coating of Zn for improving corrosion resistance [12], or investigated the characteristics of Zn coatings [13,14]. Li et al. [13] deposited pure Zn on stainless steel using two different carrier gas temperatures, 320 and 410 °C, with a nozzle travel speed of 80 mm/s. A dense microstructure of the Zn coating layer was reportedly created on the steel. Nanocrystalline grains were formed in the coating near the interface, and they severely deformed the particles, leading to the recrystallization of elongated grains. Moreover, spherical particles were observed as a result of the jetting of melted particles, which can occur in soft materials with a low melting point and intensive deformation during cold spraying [13]. In another study, Maledi et al. [14] investigated the effect of processing parameters on the mechanical and microstructural properties of mild steel coated with Zn. They performed coating in the gas temperature range of 450–550 °C and at gas pressures of 0.69 and 0.8 MPa, with different standoff distances of 15 and 25 mm/s. They found that increasing the temperature and pressure of the carrier gas could improve the bond strength between Zn and steel, decreasing the residual stress. However, in terms of hardness, no significant changes were found when these parameters increased [14]. These limited studies on the cold-spray deposition of Zn used increased gas temperatures to achieve successful coating. However, contradictory results were reported by Legoux et al. [15], who studied the effect of carrier gas temperature on the surface temperature and deposition efficiency [15]. They determined a relationship between the particle velocity and gas temperature for three different coating materials, including Zn, and their impacts on the deposition efficiency. They showed that for the Zn coating material, the deposition efficiency decreased with increasing surface temperature owing to the low melting-point temperature of Zn [15]. In our recent work [7], for the first time, we reported the in situ monitoring results of strain evolution in a Mg AZ31B substrate, where Zn was employed as an intermediate layer between the substrate and Al7075 as a top coating. The research outcome highlighted the effect of the high-CTE Zn interlayer on increasing the compressive strain in the substrate of the coated sample [7].

In this study, we examined the cold-spray deposition of pure Zn on an AZ31B-H24 Mg sheet for investigating the possibility of using Zn as the interlayer between a Mg substrate and Al7075 coating to minimize the detrimental effect of thermal mismatch and developed residual stress. Earlier studies showed that tensile residual stresses in a Mg substrate coated by Al7075 accelerated cracking, thus limiting fatigue life improvements [16]. First, by using a theoretical model, the critical and particle impact velocities of Zn powder were calculated for different carrier gas temperatures to select the coating parameters. To reduce the negative impact of the coating temperature on the Mg substrate [8], the coating temperature was minimized to maximize the compressive residual stress. It is noted that the “coating temperature” includes carrier gas temperature, exposure time, and impacted-induced temperature. Next, the Zn/AZ31B coated samples were examined to establish appropriate physical coating properties, such as thickness and surface roughness. The phase identifications of the coated samples were obtained using X-ray diffraction (XRD) to investigate the probable intermetallic phases at the interface area for different treated samples. The effects of Zn coating on the microstructure and residual stress formation in Mg substrates were also studied. Finally, the effect of a Zn interlayer on the residual stress development in Al7075/Zn/AZ31B-coated samples was investigated to determine the role of thermal mismatch in coating temperature-sensitive materials.

2. Experimental procedure

2.1. Materials and methodology

Several 30 mm × 50 mm rectangular specimens of 3.16-mm-thick AZ31B-H24 Mg alloy sheets were used as the substrate samples. The samples were heat-treated based on the ASM-recommended procedure (260 °C/15 min) to release any initial residual stresses [17]. The feedstock powder used in the experiments was an irregularly shaped commercial pure Zn powder, supplied by Centerline Ltd., Windsor, with an average size of 35 μm. Particle size measurements were performed using Mastersizer 2000 (Malvern, UK). Spherical-shaped Al7075 powder, supplied by Centerline Ltd., Windsor, with the average diameter of 23 μm (measured using Retsch technology, Camsizer XT, Germany) was used for coating. The morphologies of the Al7075 and Zn powders as well as the size distributions of the Zn and Al7075 powders are shown in Fig. 1a, b and c, respectively.

A commercial low-pressure cold-spray system manufactured by Supersonic Spray Technologies (SST) Series P Centerline, Windsor, Canada, was used to conduct the coating process. For all experiments, coating deposition was done in a single pass (single layer). To create a coating layer of Zn on the Mg substrate, Zn particles were accelerated using nitrogen gas as the propellant under a low pressure of 1.38 MPa with the standoff distance of 15 mm. The experiments were performed under a constant feed rate of 8 g/min, while the carrier gas temperature and nozzle speed were varied. Table 1 lists the various gas temperatures and nozzle speeds as the most significant parameters for studying the effect of parameters on the physical and mechanical properties of the coating and substrate. The gas temperatures were determined using analytical calculations (Section 3.1). After determining the optimum conditions for depositing Zn on Mg, Al7075 powder was coated onto the Zn/Mg samples. The standoff distance for this coating was reduced to 12 mm, and the carrier gas temperature was increased to 400 °C with a slower nozzle speed of 2 mm/s. In this series of experiments, the feed rate was 8 g/min, and the carrier gas pressure was 1.38 MPa. For comparison, the same coating process parameters were used to deposit Al7075 on the AZ31B substrates.

2.2. Residual stress measurement

To measure the residual stress distribution through the depth of the coated samples, a hole-drilling machine (Sint Technology, Restan MTS3000, Italy) with the high speed of 400,000 rpm, equipped with an air turbine was employed. Three-element strain rosettes (FRAS-2 Tokyo Sokki, Japan) were installed on the sample surface, where the residual stress was measured. To release the strain of the coated sample, a small shallow hole was mechanically drilled using a 2-mm-diameter drill bit to the depth of 1.8 mm at the center of the rosette. The strain relaxation was recorded during drilling and then analyzed based on the nonuniform method using the EVAL software to calculate the residual stress of the coated samples.

2.3. Microstructural analysis

Field emission scanning electron microscopy (FE-SEM; Zeiss Leo UltraPlus) with energy dispersive X-ray spectroscopy (EDS; Oxford Instruments) and electron microscopy (TESCAN VEGA3) were employed to analyze the microstructure and chemical composition of the interface. For these measurements, the sample cross-sections were polished and etched to reveal the grain structure of the Mg alloy samples. Details of sample preparation are described in [8].

To study the phases at the Zn/Mg-coated sample interfaces, a Bruker D8-Discover equipped with a VÅNTEC-500 area detector and Cu-Kα radiation at 40 kV and 40 mA was employed. During the measurement, a 300 μm collimator was used to scan the area in the 2θ angle mode from 20° to 95° in increments of 15°, with the exposure time of 60 s. The

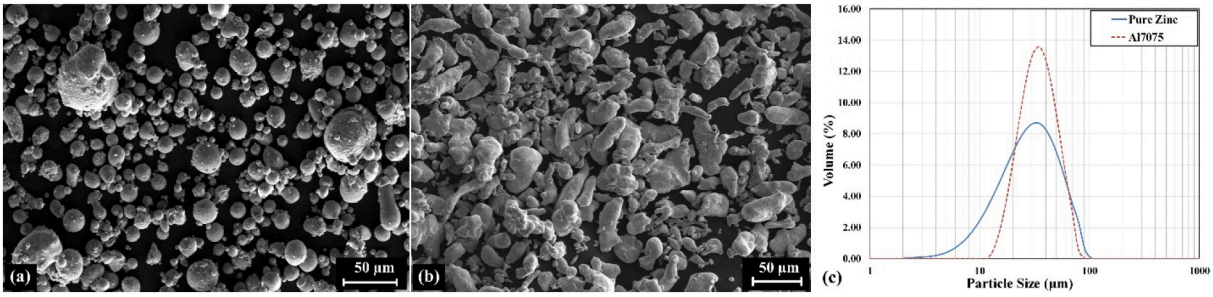

Fig. 1. SEM image of a) Al7075 and b) pure Zn powder; c) Particle size distributions for pure Zn and Al7075.

Table 1
Cold spraying parameters used in the design of experiments.

Test #	1	2	3	4	5	6	7	8	9	10	11	12
Gas Temperature (°C)	250	200	150	100	250	200	150	100	250	200	150	100
Nozzle Speed (mm/s)	5	5	5	5	10	10	10	10	15	15	15	15

obtained data were analyzed using Bruker DIFFRAC.EVA software.

A Keyence VK-X250 confocal laser microscope manufactured by Keyence Corporation, Osaka, Japan, was used to measure the surface roughness (Sa) and thickness of the coating.

In addition, the microhardness values of the samples in three different locations, namely coating layer (about 150 μm above the interface), interface, and substrate (about 150 μm below the interface), were determined on the cross-sections of the coated samples (Clemex Technologies Inc., Longueuil, Canada). Several micro-indentations with 10 g loads for 10 s (using a micro-Vickers indenter) were applied on the polished surface of the coated samples, which were treated with different carrier gas temperatures and nozzle speeds. Note that the interface is only a few hundred nanometers in size; however, the indentation area covered both the substrate and coating that comprised the interface.

2.4. Three-point bending fatigue test

Three-point bending fatigue tests were conducted using an Instron 8872 servo-hydraulic axial test frame equipped with a 3-point bending fixture. The load capacity of the machine was 25 kN, and the tests were performed at an ambient temperature. Several rectangular coated samples with dimensions of 12.7 mm × 120 mm × 6.2 mm were prepared for the bending fatigue tests. Based on the ASTM D5947 test method, the distance between the supporting spans was adjusted to 16 ± 1 times the thickness, which was approximately 100 mm. However, this span distance was not appropriate for completion of the tests, resulting in a large bending radius and failure. Therefore, the snap distance was decreased to 80 mm, and the bending tests were conducted with the R ratio of 0.1 and frequencies of 1 and 3 Hz for the low- and high-cycle fatigue tests. These series of tests were completed for the AZ31B-H24 Mg alloy samples as well as the Zn-coated samples.

3. Results and discussion

3.1. Carrier gas temperature

Gas temperature is one of the most critical parameters that can directly affect the characteristics of the coating as well as residual stress development in the coated sample. Earlier studies suggested a high temperature range (450–550 °C) for creating a stronger bond between the Zn coating and steel substrate [14]. A high-temperature coating is reasonable when the process is conducted on substrate materials with high strength and high melting point, such as steel. However, in the case of those with low melting point, such as Mg, an increase in the coating temperature can be problematic and have adverse effects on the mechanical properties and microstructures of the coated samples. Therefore, in this study, the proper gas temperature range for depositing Zn on Mg AZ31B was selected by calculating the particle velocity, particle impact velocity, and critical velocity through an analytical approach.

The impact velocity is a function of the particle velocity, calculated using [2,18]:

$$v_p \approx \left(\frac{C_2}{\sqrt{RT_0}} + \sqrt{\frac{\rho_p d_p}{C_d L_d P_0}} \right)^{-1} \quad (1)$$

where vp is the particle velocity at the nozzle exit, $C_2(0.42)$ is a constant for nitrogen as a process gas, R is the universal gas constant, T_0 is the gas temperature, ρ_p is the density of the particle material, d_p is the particle diameter, C_d is the drag coefficient, L_d is the length of the divergent part of the nozzle, and P_0 is the stagnation pressure. The drag coefficient is a function of the particle's Mach number and size [18]. We estimated the drag coefficient for 35 μm particles, which is the average particle size of the material used in this research, and it was assumed to be constant at each temperature for all particle sizes. Moreover, the particle impact velocity was obtained using:

$$v_{pi} = v_p \left(1 + \frac{\rho_0 \delta}{\rho_p d_p} \right)^{-1} \quad (2)$$

where ρ_0 is the gas density, and δ is the characteristic thickness of the bow shock boundary layer. The impact velocity was noted to be influenced by the bow shock effect, which is related to the nozzle standoff distance. Here, δ was calculated using the relations presented by Pattison et al. [19].

Fig. 2a depicts the Zn particle velocity at different carrier gas temperatures with respect to the particle size. At a constant temperature, the particle velocity decreases with increasing particle size; however, a similar trend was observed for all selected temperatures, as shown in Fig. 2a. Based on the graph, with increasing gas temperature from 100 to 250 °C, the particle velocity of the 35-μm Zn particles changed by only around 50 m/s. Fig. 2b compares the particle, impact and critical velocities with respect to the particle size at the gas temperature of 100 °C. This graph illustrates that the particle and impact velocities follow different trends for particles smaller than 10 μm; however, by increasing the particle size, particularly for the 35-μm particles, both velocities remained almost the same.

In addition, the critical velocities of various sizes of Zn particles were calculated at the gas temperature of 100 °C. Eq. (3) [18] expresses the critical velocity, which is a function of the particle's properties and

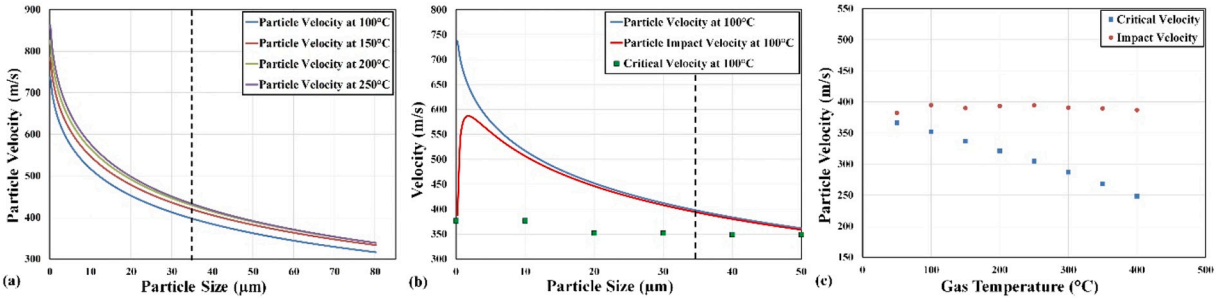

Fig. 2. Particle size, velocity, and temperature interactions: a) Particle velocity at the nozzle exit; b) Particle, impact and critical velocity vs. particle size at 100 °C; c) Critical and impact velocities of pure Zn particles with an average size of 35 μm at different gas temperatures.

particle temperatures:

$$v_{cr} = K_1\sqrt{Cp(T_m - T_p) + 16\frac{\sigma_{UTS}}{\rho_p}\left(\frac{T_m - T_p}{T_m - 293}\right)} \quad (3)$$

where C_p is the specific heat capacity of a particle, T_m is the melting temperature of a particle, T_p is the impact temperature of a particle, σ_{UTS} is the ultimate tensile strength, and K_1 is a fitting parameter [18]. The particle impact temperature (T_p) for this calculation, which depends on the particle size, were obtained using the relations reported by Mauer et al. [20].

The results of critical velocity calculation at temperature of 100 °C respecting the particle size in Fig. 2b, show a slight decrease with increasing the particle size, and justify debonding for the particles bigger than 50 μm at the low temperature.

Fig. 2c shows the critical velocity with respect to temperature for the 35 μm Zn particles for the gas temperature range of 50–400 °C. Based on this graph, with an increase in the carrier gas temperature, the temperature of the particles increases, decreasing the critical velocity. For comparison, the particle impact velocity of 35-μm Zn particles based on temperature is superimposed on Fig. 2c. The graph reveals that the impact velocity of the particle is greater than the critical velocity of Zn particles at all temperatures above 50 °C. This suggests that successful deposition may be achieved at any temperature above 50 °C. Hence, for this study, the range of the carrier gas temperature was only considered to be from 100 to 250 °C. We further verified that a very thin layer of Zn coating with low deposition deficiency could be formed at 50 °C.

3.2. Surface roughness and thickness

Several coating trials based on the coating parameters (Table 1) were performed to establish a link between the processing parameters and coating characteristics. Fig. 3 summarizes the results for the coating roughness and thickness as functions of carrier gas temperature and nozzle speed while the other process parameters (carrier gas pressure and feed rate) remained constant. Fig. 3a depicts the effect of the coating process variables on the coating thickness. By increasing the carrier gas temperature for all nozzle speeds, particularly for 5 mm/s, the deposition thickness was increased. This phenomenon can be attributed to the critical velocity, which decreases with an increase in temperature (Fig. 2c), resulting in a larger volume of particles reaching and exceeding the critical velocity and adhering to the substrate to create a thicker coating. The same trend was observed in the relationship between temperature and surface roughness (Fig. 3b). An increase in the carrier gas temperature results in an increase in the temperature of the substrate and particles, providing enhanced local ductility. This increased ductility will, in turn, intensify local deformation upon impact, increasing both material jetting and surface roughness.

Fig. 3c illustrates a monotonic relation between the thickness of the coating layer and surface roughness. A similar observation was reported by Tan et al. [21], who coated Ti6Al4V on a Ti6Al4V substrate. They

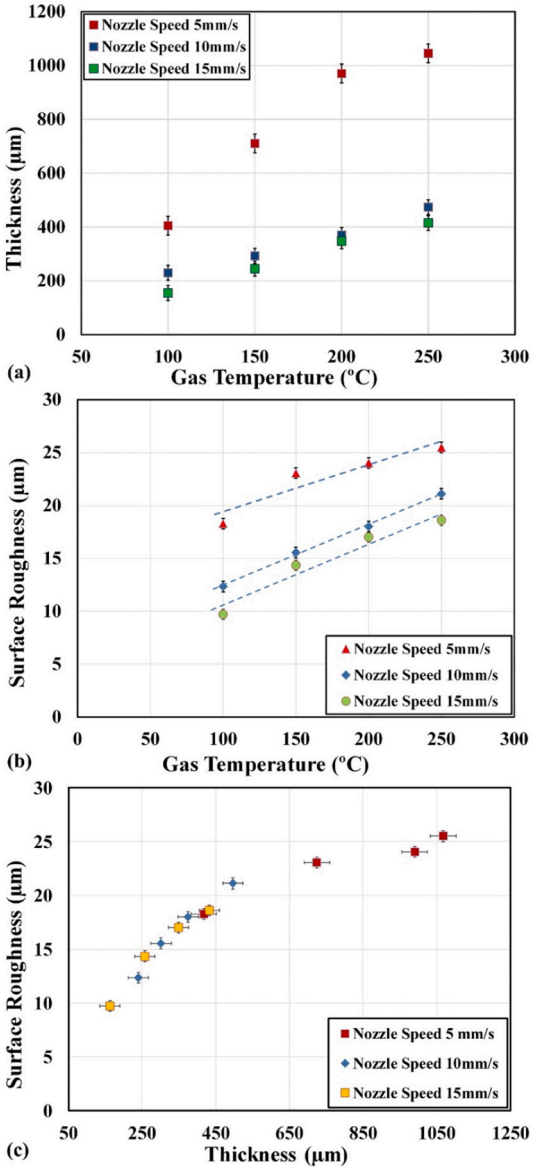

Fig. 3. Relation among the gas temperature, nozzle speed, and coating roughness and thickness characteristics: a) Average coating thickness with respect to carrier gas temperature; b) Average surface roughness with respect to carrier gas temperature; c) Average surface roughness based on average coating thickness for different nozzle speeds (5, 10, and 15 mm/s).

reported that the porosity increased owing to the thickening of the coating by recoating the surface, resulting in an increase in the surface roughness. In this study, the coating layer thickness was changed at each nozzle speed by changing the carrier gas temperature. A higher gas temperature provides more kinetic energy for the particles, leading to a more powerful impact as well as enhancing the ductility of Zn particles and deposited material. These phenomena can promote material jetting, and consequently, particle trapping on the surface [22]; this could be another reason for the monotonic relation between the thickness and surface roughness.

3.3. Microstructure of Zn coating and AZ31B substrate near the interface

Next, we investigated the effect of the coating processing parameters on the coating and substrate microstructural characteristics, which in turn affect the mechanical properties of the coated samples. Fig. 4 shows the cross-sectional microstructure of the coating layer deposited at the constant nozzle speed of 10 mm/s and carrier gas temperatures of 100 and 250 °C. At lower temperatures, the coating structure mainly comprised lamellar grains formed by intensive deformation of the Zn particles during coating (Fig. 4a). However, the coating layer deposited at a higher temperature (Fig. 4b), despite the fact that the particles were more susceptible to deformation, exhibits relatively less elongation, more trapped particles, along with a lamellar microstructure. The reason may be attributed to the higher deposition rate at higher gas temperatures (Fig. 3a). In this case, the deformation of the particles is restricted by the presence of more adjacent particles that are deposited at the same time, with more particles being trapped within others. The trapped particles can be considered as a source of defects in the coating because free spaces remain around these particles owing to their structures [22]. One such trapped particle is shown in Fig. 4c. In this case, the particles were deposited successively over the trapped particle while leaving a gap at the boundary. This defect creates an area within the coat with lower cohesion strength, as observed by the unbonded boundary of the trapped particle with nearby splats; this in turn, degrades the mechanical strength of the coated samples.

The effect of cold-spray deposition on the microstructure of the substrate can be significant, particularly for relatively soft materials with a low melting point, for example, Mg AZ31B. While Zn is also a soft material with a lower melting point, its high density result in a high impact energy during coating; this may damage the microstructure of the substrate near the interface. Generally, the energy of each impact and number of impacts per unit time (peening effect), as well as the coating temperature, are the critical factors affecting the microstructural changes of the substrate [4]. In the case of Mg, exposure to a relatively high temperature during cold-spray coating can be more influential, and high-temperature microstructural changes, such as recovery, dynamic recrystallization, and even dynamic grain growth, may occur during coating [4,8]. Hence, the investigation of the microstructural changes of the substrate is essential.

Fig. 5 shows the microstructure of the Mg substrate in the vicinity of the interface for different processing conditions. As observed, two regions are distinguishable: the first region with very fine grains just below the interface, followed by a second zone comprising coarser grains. The boundary between these two regions is highlighted in Fig. 5a. The images in each row and column of this figure were captured at various gas temperatures and nozzle speeds, respectively. In the first row (Fig. 5a–c) and at 100 °C, for example, an increase in the nozzle speed evidently decreases the width of the fine-grain area (see in Table 2). Furthermore, coarser grains are formed in the second zone as a result of reducing the number of impact particles. This trend was repeated for all temperatures. For a constant nozzle speed, the fine-grain area is observed (e.g., Fig. 5c, f, i) to be reduced by increasing the carrier gas temperature.

In the coarse-grain zones, two types of grain structures were formed. For the higher temperature process, dynamic grain growth showed a predominant grain structure directly after the grain refinement zones, as observed in Fig. 5g, j, and k. Moreover, with decreasing thermal energy, the prevailing peening effect caused a decrease in the grain size in the second zone (Fig. 5d). The size of the grains in the second area was altered by changing the coating parameters and depends on the interaction between thermal and peening effects. The maximum grain size of this region was observed in the case of 100 °C and 15 mm/s, with the minimum coating temperature and minimum material deposition (Fig. 5c). In contrast, the minimum grain size for this region (the second area) was observed in the sample coated at 150 °C and 5 mm/s; this was because the velocity of particles was high enough to produce the maximum peening effect and the temperature was low enough not to change the microstructure (Fig. 5d).

3.4. Phase identification

To identify the potential formation of intermetallic compounds between Zn and Mg, an EDS line scan and XRD were used to trace material mixing and phases at the interface. Fig. 6a shows an SEM image of the interface when the sample was treated at the carrier gas temperature of 250 °C with the nozzle speed of 5 mm/s (test #1), and Fig. 6b shows the chemical composition analysis of the coating, interface, and substrate layers detected through the EDS line scan. This SEM image and chemical analysis confirmed the mixing of Mg and Zn, and the formation of a distinguishable interface region. Usually, the interface region of the cold-spray-coated sample is a thin layer in the range of a maximum of a few hundred nanometers. However, based on the SEM and EDS results in

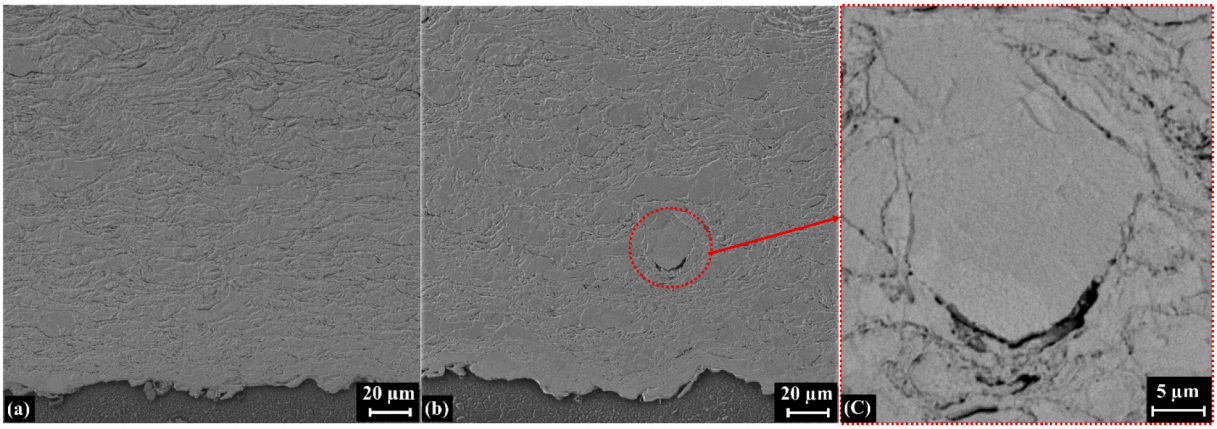

Fig. 4. Cross-sectional microstructure of Zn coatings at the constant nozzle speed of 10 mm/s and carrier gas temperatures of a) 100 °C and b) 250 °C; c) high-resolution image of the defect in Zn coating at 250 °C.

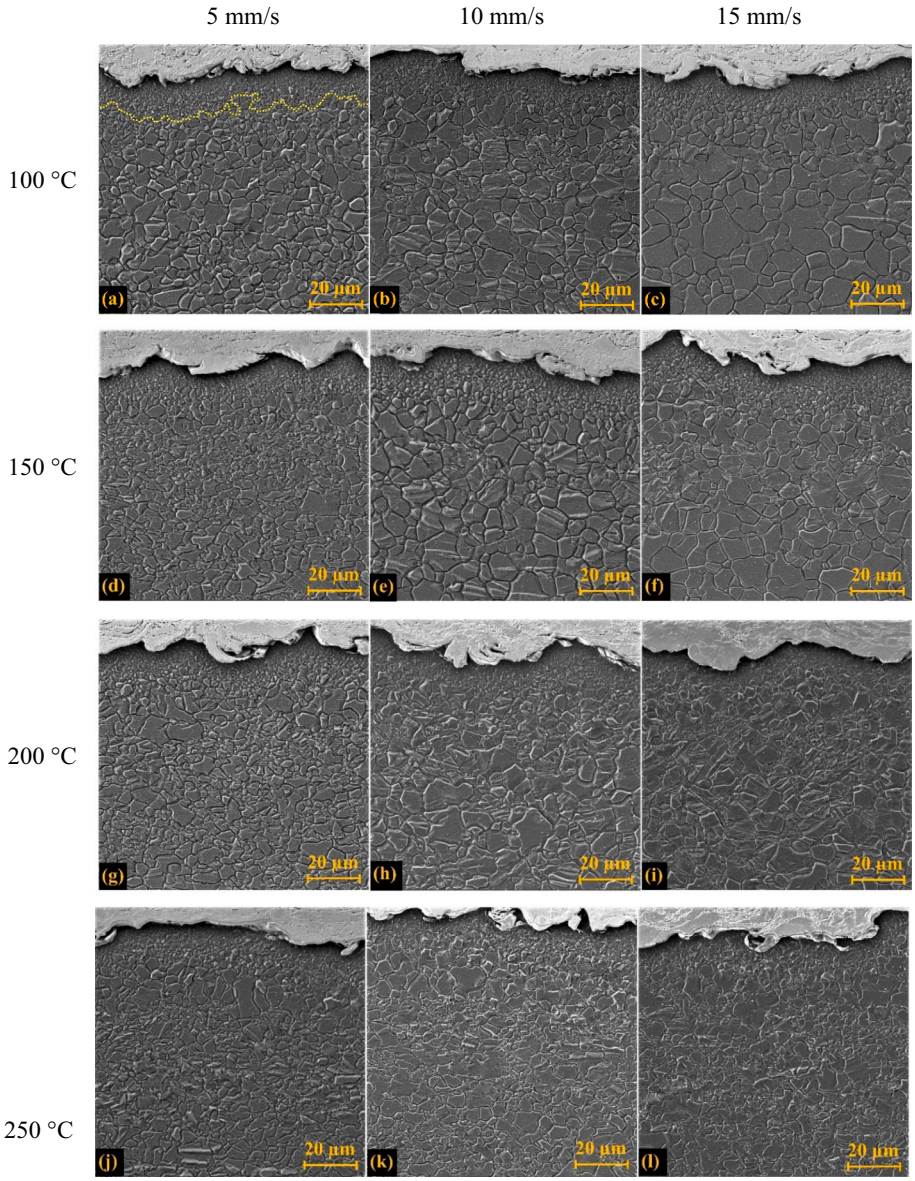

Fig. 5. SEM images showing microstructures of Mg alloy-coated substrate samples at the respective nozzle speeds of 5, 10, and 15 mm/s for gas temperatures of: a, b, c) 100 °C; d, e, f) 150 °C; g, h, i) 200 °C; and j, k, l) 250 °C.

Table 2
Average of the fine-grain area's width for 12 samples.

Gas temperature (°C)	Nozzle speed (mm/s)	The width of fine-grain area (μm)
100	5	11.62 ± 0.92
100	10	6.13 ± 0.54
100	15	4.27 ± 0.45
150	5	9.16 ± 0.82
150	10	7.70 ± 0.42
150	15	6.19 ± 0.47
200	5	8.40 ± 0.34
200	10	6.51 ± 0.35
200	15	3.94 ± 0.20
250	5	6.44 ± 0.58
250	10	3.76 ± 0.20
250	15	3.19 ± 0.44

Fig. 6, the interface thickness formed during the cold-spray coating of Zn on AZ31B is in the range of a few microns. The nature of the interface depends on the properties of the two materials as well as the coating processing parameters, such as pressure and temperature. Various types of interfaces, including no-mixing and mixed zones of the two materials, can be found in the different cases. The crystal structure of the mixed zone of the interface in the cold-spray-coated samples has been studied earlier, resulting in the observation of amorphous phases [23,24], nanocrystalline phases [13,25], and the formation of intermetallic phases [26]. The interfaces between the coating and substrate layers of all 12 samples, as listed in Table 1, were examined through XRD to determine the structure of the interface region. The conclusions of this study are presented in Table 3. The results demonstrate that different intermetallic phases were formed under various combinations of temperatures and nozzle travel speeds; these results reveal the possibility of mixing the substrate and coating layers and support the EDS line scan results. For instance, the ratio of Mg/Zn at the interface region for test #1 (Fig. 6b) is around the ratio of these elements for the intermetallic $Mg_{51}Zn_{20}$ detected using XRD (Table 3). As the coating temperature increases with an increase in the carrier gas temperature and/or decrease in the nozzle travel speed, the ratio of the carrier gas temperature to nozzle speed was considered as an index for the coating temperature. To evaluate the relationship between the ratio of carrier gas

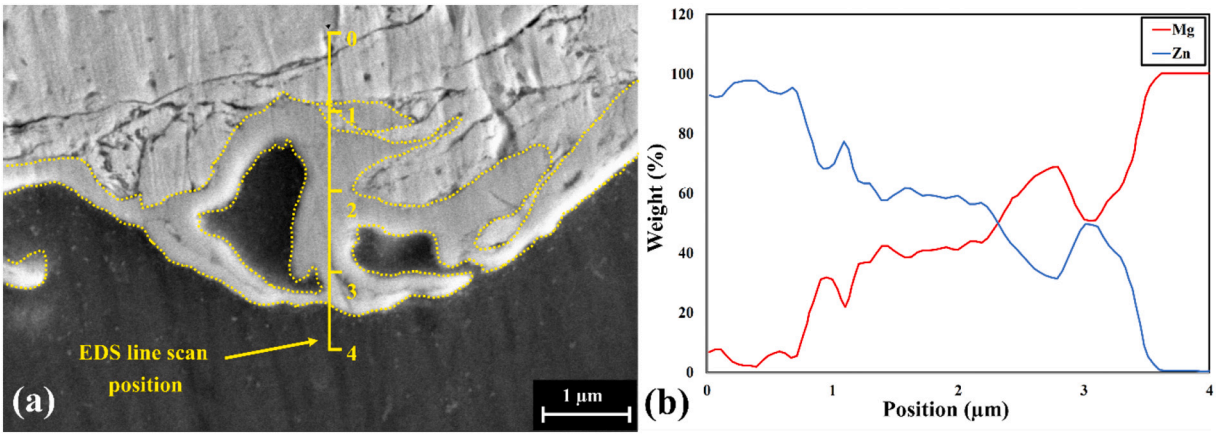

Fig. 6. a) SEM image of the interface showing the formation of the interface region between the coating and substrate layers. b) EDS line scan results showing chemical composition changes across the interface.

Table 3
Phase identification for the interfaces of Zn coating on AZ31B at different nozzle speeds and under various carrier gas temperatures.

Gas temperature (°C)	Nozzle speed (mm/s)	Phase	Crystalline structure	Mg/Zn
100	5	$Mg_{51}Zn_{20}$	Orthorhombic	2.55
100	10	$Mg_{0.97}Zn_{0.03}$	Hexagonal	32.33
100	15	$Mg_{0.97}Zn_{0.03}$	Hexagonal	32.33
150	5	Mg_2Zn_{11}	Cubic	0.18
150	10	$Mg_{0.97}Zn_{0.03}$	Hexagonal	32.33
150	15	$Mg_{0.97}Zn_{0.03}$	Hexagonal	32.33
200	5	$MgZn_2$	Hexagonal	0.50
200	10	$Mg_{21}Zn_{25}$	Trigonal	0.84
200	15	$Mg_{0.97}Zn_{0.03}$	Hexagonal	32.33
250	5	$Mg_{51}Zn_{20}$	Orthorhombic	2.55
250	10	$MgZn_2$	Hexagonal	0.50
250	15	$Mg_{51}Zn_{20}$	Orthorhombic	2.55

temperature /nozzle speed and synthesized intermetallic phases, the Mg/Zn ratios of the intermetallic phases formed at the interface of each coating condition were plotted with respect to the carrier gas temperature /nozzle speed (Fig. 7). This graph indicates a specific trend for creating intermetallic phases at the interface of Mg/Zn-coated samples. When the ratio of carrier gas temperature to nozzle speed is lower than approximately 16 °C s/mm, a metastable intermetallic phase of Mg-rich $Mg_{0.97}Zn_{0.03}$ is formed. However, when the ratio of carrier gas temperature to nozzle speed is greater than this value, Zn-rich phases are detected at the interface. Fig. 7 reveals that both the carrier gas temperature and nozzle travel speed are decisive factors that play crucial roles in the phase formation. For example, when the carrier gas temperature was 100 °C, which is the minimum temperature considered in this study, and the nozzle speed was 5 mm/s, a high-temperature intermetallic phase ($Mg_{51}Zn_{20}$) was formed. In contrast, during coating at the carrier gas temperature of 200 °C and nozzle travel speed of 15 mm/s, a low-temperature intermetallic phase of the $Mg_{0.97}Zn_{0.03}$ phase was developed.

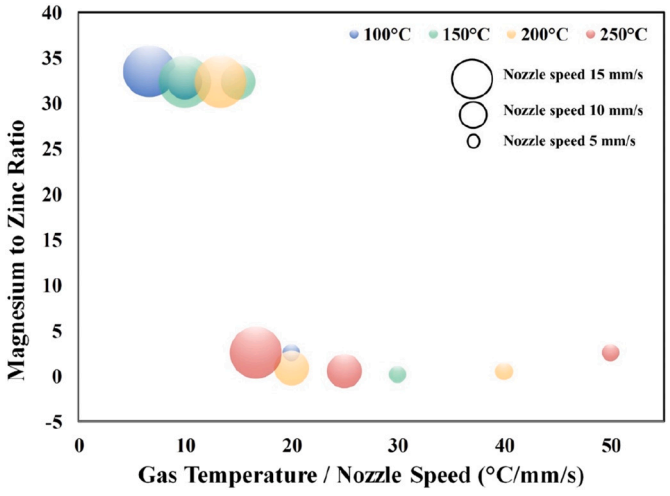

Fig. 7. Ratios of Mg/Zn in the intermetallic phases formed at different temperatures based on the ratio of carrier gas temperature to nozzle speed. (The bubble sizes represent the nozzle speeds.)

In the solid-state cold-spray condition, with the temperature much lower than the particle melting point, the thermal energy and time required for intermetallic phases to be synthesized by a solid-state diffusional process are insufficient [27,28]. In contrast, the mixing of the substrate and coating material in the liquid state is a fast process, and the intermetallic phase can nucleate and grow during solidification: the probable mechanism for intermetallic formation during Zn coating on Mg. The idea of partial melting and intermetallic-phase formation at the interface of the particle/substrate has been reported in previous studies [25,27,29,30–35]. For example, King et al. demonstrated the formation of a $CuAl_2$ intermetallic phase during the cold-spray deposition of copper on *Al* through computer simulations and experimental observations. They reported that the melting of copper particles was not achievable with the coating process parameters used in their experiments. However, they considered the possibility of the formation of a low-melting-point eutectoid phase at the interface, which can be melted, and that $CuAl_2$ intermetallic phases may grow in this liquid media [32].

To evaluate the intermetallic-phase formation through melting and solidification mechanisms, a high resolution imaging (e.g., TEM [36]) examination of the interface is required, which is out of the scope of the current study. However, the surface of the coating was observed under different coating conditions in search for traces of resolidified Zn particles that might have ejected from the interface and/or earlier coating layers due to the material jetting and landed on the coating surface. Fig. 8a and Fig. 8b show the small spherical droplets on the surface coating, formed at 250 °C with the nozzle speed of 5 mm/s at two different magnifications. When the carrier gas temperature was 100 °C with the nozzle speed of 15 mm/s, the same spherical droplets were observed; however, their size and number were significantly reduced (Fig. 8c). Observations of similar droplets of Zn have also been previously reported [12,13]. Li et al. reported the formation of small spherical Zn particles of several hundreds of nanometers on the coating surface of cold-spray-deposited Zn on steel. They claimed that these particles formed during the deposition because their size was much smaller than

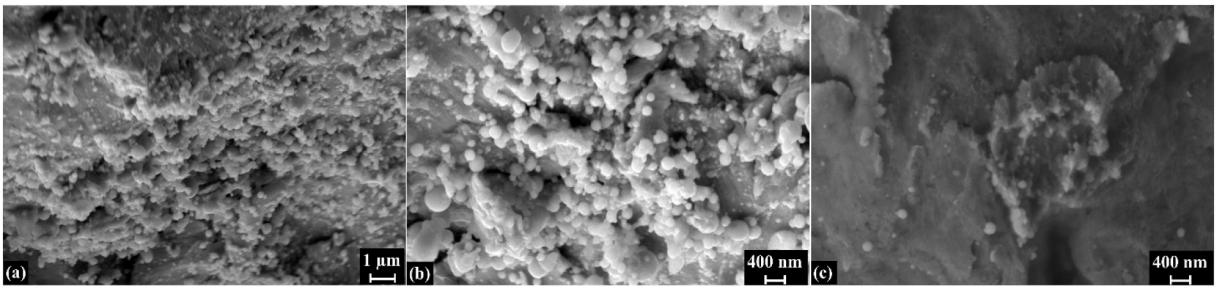

Fig. 8. a) Low- and b) high-magnification SEM images of morphologies of resolidified partially melted particles during jetting on Zn coating surface at the gas temperature of 250 °C and nozzle speed of 5 mm/s. c) Sparse resolidified partially melted particles at the coating surface at 100 °C and 15 mm/s.

the original powder. In addition, the spherical shape of the particles was considered evidence of partial melting and solidification during the coating process that implies the formation of liquid phase at the interface [13,37]. Together, SEM and XRD analyses provide important insights into the formation of intermetallic phases at the Zn/Mg interface during cold-spray coating. A sufficiently high thermal energy of particles was created during the impact of the soft material with a low melting temperature. This can increase local strain beyond the damage limit, leading to the spattering of the highly strained and partially melted particles from the edge, material jetting, and formation of spherical droplets on the surface. Based on the XRD analysis, at low temperatures, the chance of mixing Mg and Zn is low; therefore, the metastable Mg-rich $Mg_{0.97}Zn_{0.03}$ devitrifies from the liquid during solidification. By increasing the ratio of carrier gas temperature to nozzle speed, the impact energy becomes sufficient for mixing Mg and Zn; hence, different intermetallic phases grew at the interface.

3.5. Hardness measurements

Hardness measurements were conducted at the substrate, coating, and interface layers, as explained in Section 2.3. Table 4 lists the hardness data of these layers for the Zn/AZ31B-coated samples at the constant nozzle travel speed of 10 mm/s and different carrier gas temperatures. Here, each data point is the average of eight hardness measurements. The comparison of the interface hardness for different carrier gas temperatures reveals similarities in the hardness values at temperatures of 100 and 150 °C; this can be attributed to the formation of the same intermetallic $Mg_{0.97}Zn_{0.03}$ phase (Table 3). The metastable $Mg_{0.97}Zn_{0.03}$ crystal structure and its mechanical properties might be similar to those of Mg [38], resulting in an interface hardness similar to that of the Mg substrate under low carrier gas temperature. However, the increase in the carrier gas temperature to 200 and 250 °C increased the interface hardness. As mentioned earlier, $Mg_{21}Zn_{25}$ and $MgZn_2$ were detected at the interface at 200 and 250 °C, respectively. $Mg_{21}Zn_{25}$ has a trigonal crystal structure with a hardness of 4.66 GPa, while $MgZn_2$ has a hexagonal C14 Laves crystal with hardness of 5.08 GPa [39], and the respective hardness values of the interface of the coating layers at 200 and 250 °C are 113 and 124 HV, which are equivalent to 1.1 and 1.2 GPa, respectively. The decreased hardness of the interface compared with the intermetallic hardness could be because of the intermetallic compounds embedded in the matrix of Zn and Mg. Note that the intermetallic phases were embedded in the interface region, which is smaller than the indent footprint. The data reported here present the average values of the hardness of the Mg substrate close to the interface, mixed interface region, and Zn coating adjacent to the interface. Moreover, higher carrier gas temperature of 250 °C led to increased melting; thus, increasing the chance for intermetallic-phase formation of $MgZn_2$ with a higher hardness.

Table 4
Average hardness data of coating, interface, and substrate layers near the interface at different gas temperatures with a constant nozzle speed of 10 mm/s.

Gas temperature (°C)	100	150	200	250
Coating (HV)	38.67 ± 0.72	41.67 ± 3.14	56.67 ± 2.37	43.33 ± 2.33
Interface (HV)	61.33 ± 1.78	60.33 ± 3.07	113.00 ± 7.59	124.67 ± 7.09
Substrate (HV)	73.67 ± 0.98	78.33 ± 0.98	60.00 ± 2.16	65.00 ± 2.45

In addition, the effect of the carrier gas temperature on the coating and substrate hardness can be justified by considering the grain size of the indent (Fig. 5) and another two competitive processes: peening and annealing. Generally, a decrease in the grain size increases the hardness. Moreover, an increase in the carrier gas temperature leads to increased particle kinetic energy, resulting in an improved peening effect and greater hardness [40]. Furthermore, a rise in temperature is well-known to reduce the hardness due to stress relief and annealing effects [41]. Based on the data presented in Table 4, and as far as hardness is concerned, the carrier gas temperature of 200 °C seems to be the optimum deposition condition and the temperature at which the maximum hardness was measured in the coating. However, for the substrate, the maximum hardness was measured below 150 °C, which can be attributed to the smaller grain size of the indented area in these two sets of samples compared with those at 200 and 250 °C, where large grains formed after coating, as shown in Fig. 5.

3.6. Fatigue performance of coated samples

Intermetallic phases are usually brittle, which may weaken the mechanical performance of Zn-coated AZ31B parts for a long-term service. To evaluate the performance of the coated samples, the fatigue life values of the stress-relieved AZ31B samples and coated samples at 250 °C were investigated. Thirty flat samples with and without Zn coating were tested using a 3-point bending fixture and a positive R ratio of 0.1 to provide a tension–tension state of stress on the coating. For this test, the maximum and minimum loads were controlled to reach the maximum and minimum defined stress levels on the sample. The failure criterion for the load-controlled tests was considered as the final fracture. The correlation between the stress and load was defined using a well-known 3-point bending flexural strength equation.

Fig. 9a shows the fatigue results of uncoated AZ31B and Zn-coated samples at 250 °C. The fatigue failure of the coated samples in the low- and high-cycle regimes occurred for a lower number of cycles compared with the stress-relieved Mg alloy samples. The decrease in the fatigue life of the AZ31B samples after Zn coating may be attributed to the lower fatigue strength of Zn than the AZ31B Mg alloy [42,43], while the maximum stress was applied to the Zn coating surface during the 3-point bending tests. However, cracks might be initiated from the interface because of the existence of brittle intermetallic phases in this region. To clarify the crack initiation of the samples, the surface of the Zn coating was monitored during the fatigue test, revealing that material

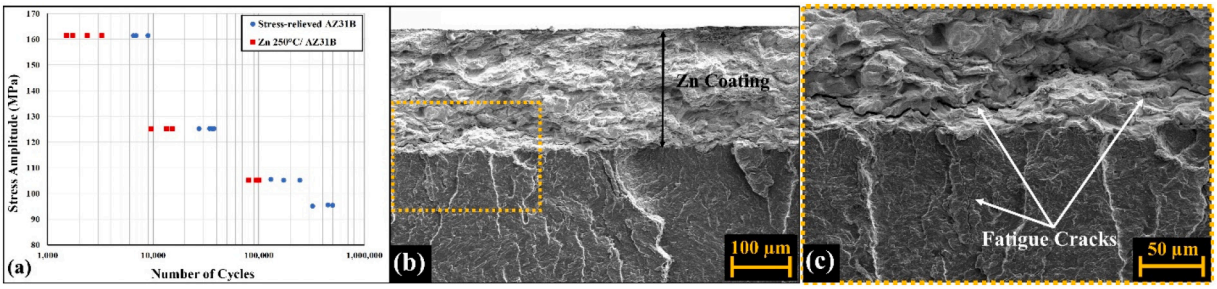

Fig. 9. a) Fatigue test results for Mg AZ31B and Zn-coated samples at the carrier gas temperature of 250 °C; b and c) SEM images of fracture surface of the 3-point bending fatigue of the coated sample after 101,200 cycles, showing propagation of the cracks at the interface under two magnifications.

deterioration (i.e., increasing the deformation at the constant applied load) started before cracks were observed on the surface of the sample. Moreover, the SEM image of the fractured surface of the sample (Fig. 9b) reveals that the fatigue cracks were initiated from the interface and propagated in the coating parallel to the interface, while there was no evidence of coating delamination. Fig. 9c shows a high-resolution image of the cracks in Fig. 9b. Moreover, the other crack in this figure nucleated at the interface and grew into the Mg layer perpendicular to the crack at the interface. Based on these observations, we conclude that the formation of brittle intermetallic phases at the interface is responsible for the lower fatigue life of the coated samples in the range of the coating parameters used in this study.

3.7. Residual stress profiles

To evaluate the effects of the processing parameters on residual stress development in the coating and substrate layers, the substrates were coated such that the thickness of the deposited materials for different processing parameters remained constant. To achieve this, by using the data presented in Fig. 3, various nozzle speeds (listed in Table 5) were selected to produce a coating with a constant thickness of 350 ± 1 µm at the target temperatures. Based on the data presented in Fig. 3, an increase in the carrier gas temperature increased the coating thickness at constant feed rate, carrier gas pressure, and nozzle travel speed. Therefore, the nozzle speed was adjusted to compensate for the effect of the increasing temperature on the coating thickness. According to the experimental design presented in Table 5, the variables affecting the residual stress development in the coating and substrate layers were limited to: 1) the kinetic energy of the particles, which was determined by the carrier gas temperature at constant pressure, and 2) the number of impacts, which was determined by the nozzle travel speed at a constant feed rate. Then, the residual stress was measured for different coating treatments.

For each coating combination shown in Table 5, four residual stresses were measured using the hole-drilling method. The overall depth of measurement in all cases was 1.5 mm. Therefore, the coating, interface, and ~ 700 µm of the substrate near the interface were included in the measurements. Fig. 10a depicts the residual stress distribution of the Mg substrate coated with Zn. As observed, the thermal energy of the process decreased by reducing the gas temperature, inducing more compressive residual stress on both the Mg side and Zn side of the interface. These residual stress changes at 100 °C (approximately −41.1 MPa) are similar to those at 150 °C (−35.5 MPa), significantly enhancing the compressive residual stress development than those for the higher temperatures of 200 and 250 °C with similar compressive residual stresses of −17.8 and − 15.2 MPa, respectively. The enhancement of residual stress at the interface can be attributed to three different phenomena, which occur simultaneously: the coating/substrate CTE mismatch, interface temperature, and impact-induced peening effect. The nozzle travel speeds for coating at 100 and 150 °C were almost the same, and this temperature range is not critical for the Mg alloy; hence, a higher compressive residual stress is expected at these temperatures than that for the coating treatments at higher temperatures. However, the nozzle travel speed of the coating at 250 °C was notably higher than that of the coating at 200 °C, which partially compensated for the high temperature of the carrier gas for the selected coating parameters at this critical temperature range. Therefore, similar residual stress can be observed for these two coating conditions (carrier gas temperatures of 200 and 250 °C). Coating at lower temperatures reduced the destructive thermal mismatch effect and the chance for microstructural relaxation of the Mg substrate. In contrast, an increase in the gas temperature transformed the residual stress on the coating surface into tensile residual stress, despite the existence of the peening effect. The development of tensile residual stress on the coating surface can be attributed to the thermal mismatch that overcomes the peening effect, which is washed out because of annealing at high temperatures [3,7,8] and occurs at higher coating temperatures.

Table 5
Processing parameters for residual stress measurements.

Gas temperature (°C)	Pressure (MPa)	Feed rate (g/min)	Nozzle speed (mm/s)	Coating thickness (µm)
100	1.38	8	6.5	350 ± 1
150	1.38	8	8.5	350 ± 1
200	1.38	8	12.5	350 ± 1
250	1.38	8	20	350 ± 1

3.8. Control of the residual stress distribution in multilayer coating

Thermal mismatch can play a crucial role in changing the residual stress induced in the cold-sprayed samples. One strategy to compensate for the detrimental effect of thermal mismatch is to deposit an interlayer of metal for engineering the CTE mismatch effect. For example, studies have reported that cold-sprayed Al7075 on AZ31B can induce tensile residual stress in the substrate near the interface, thus increasing its susceptibility to cracking and reducing fatigue life [8,16]. However, Zn has a higher CTE than Al and Mg, and thus might resolve the thermal mismatch problem. Hence, as described in this section, we studied the effect of the Zn interlayer on the residual stress development in the Al7075/Zn/AZ31B multilayer-coated samples. The processing parameters for the multilayer coating of Al7075/Zn/AZ31B were similar to the coating parameters used for Al7075 on the Mg alloy substrate, as explained in experimental procedure section.

Fig. 10b depicts the residual stress developed in the Al7075 coated on the Mg AZ31B samples. The comparison of the distribution of residual stress in the Al7075/AZ31B and Zn/AZ31B samples shows that coating the Al alloy with a lower CTE than Mg alloy changes the residual stress of the interface from compressive to tensile stress. However, when pure Zn was coated at the lowest gas temperature of 100 °C with a nozzle travel speed of 6.5 mm/s as an interlayer between the Al and Mg alloys, the three layers of Al alloy, Zn, and Mg alloy (up to approximately 400 µm) experienced compressive residual stress relative to the CTE and an

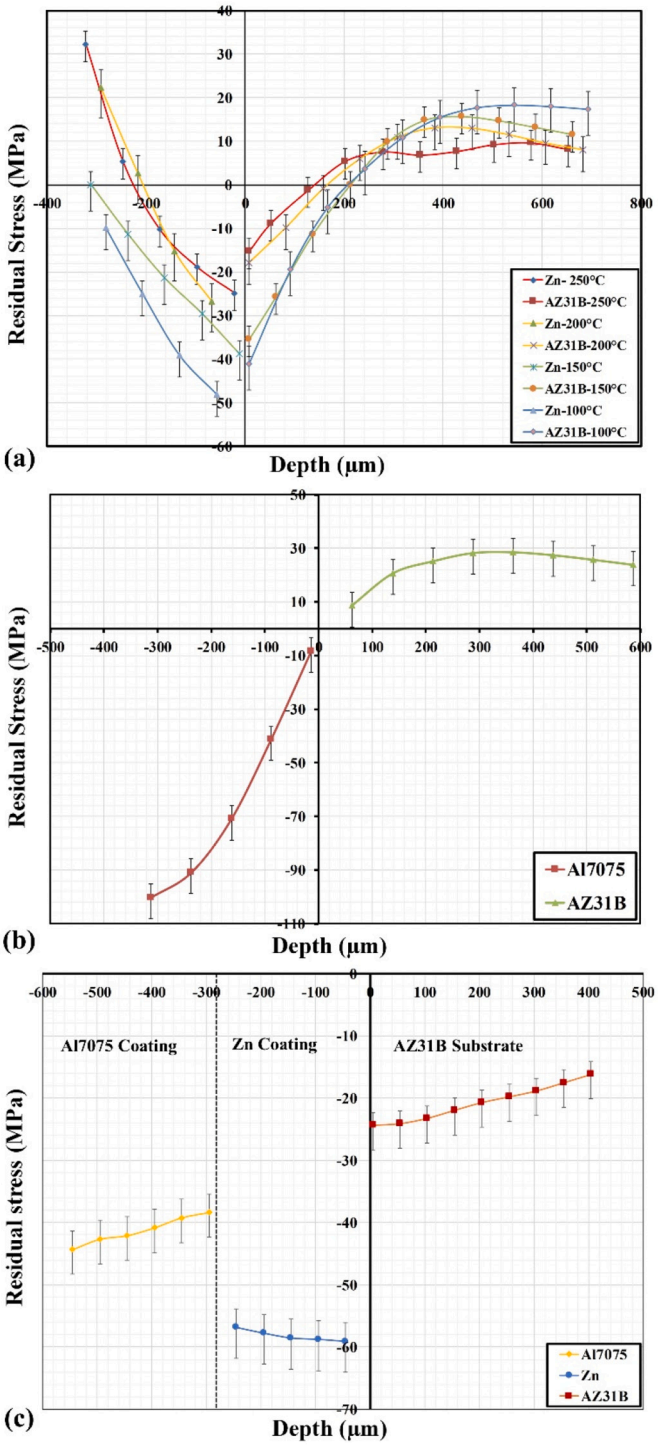

Fig. 10. Hole-drilling residual stress measurements for a) Zn-AZ31B coated samples at carrier gas temperatures of 100, 150, 200, and 250 °C; b) Al7075-AZ31B at 400 °C and nozzle speed of 2 mm/s; c) Multilayer of Al7075-Zn-AZ31 at 100 and 400 °C and nozzle speeds of 6.5 and 2 mm/s for coating Zn and Al7075, respectively.

appropriately low level of thermal energy (Fig. 10c). The same observation was reported by Marzbanrad et al. [7], who used fiber Bragg grating sensors to measure the residual strain of Mg alloy samples coated with multiple layers of Zn and Al7075 [7]. In this study, depositing a Zn interlayer between the AZ31B substrate and Al7075 coating enabled the control of the tensile residual stress in the substrate near the coating induced by Al7075 and transformed it to compressive residual stress. Because the CTE of the Zn coating is higher than those of Al7075 and AZ31B, the Zn coating was expected to experience tensile residual stress; whereas, compressive residual stress was expected in the Al7075 and AZ31B substrates. However, the peening effect of the Al7075 coating on the Zn coating overcame the thermal mismatch effect and induced significant compressive residual stress in the Zn coating as well as in Al7075 and AZ31B.

To demonstrate the impact of multilayer coating on the hardness of coatings and substrates, hardness measurements were performed at different locations of the multilayer coatings. Based on these results, the Al7075 coating has the highest hardness (133.00 ± 5.21 HV), while Zn has the lowest hardness among the coated samples (32.00 ± 1.08 HV). After the multilayer coating, the hardness of the Mg AZ31B substrate was measured to be 67.00 ± 0.41 HV. The interface between Zn and Mg AZ31B has the higher hardness (87.67 ± 1.65 HV) than that between Al7075 and Zn (72.33 ± 1.03 HV). The high hardness of the Zn and Mg interface can be attributed to the expected intermetallic phases formed in these regions during the multilayer coating of Al7075/Zn/AZ31B.

4. Conclusion

In this study, the cold-spray technology was utilized to deposit pure Zn on an AZ31B-H24 Mg sheet. The effects of the processing parameters, including carrier gas temperature and nozzle travel speed, on the physical, mechanical, and microstructural properties of the coating and substrate were investigated. Moreover, the use of Zn as an interlayer between the Mg substrate and Al7075 coating to minimize the effect of thermal mismatch on the residual stress in the coating and substrate was explored. The following major conclusions can be drawn from the results:

- Various intermetallic phases were formed at the interface of the Mg AZ31B substrate and Zn coating under different coating conditions. The results showed a relationship between the type of intermetallic-phase formation at the interface and the ratio of carrier gas temperature /nozzle speed. When the ratio of carrier gas temperature to nozzle speed was below 16 °C s/mm, a metastable phase of $Mg_{0.97}Zn_{0.03}$ could grow at the interface. However, the increase of this ratio led to the formation of different Zn-rich phases at the interface.
- The microhardness values of the coating, interface, and substrate layers were measured. The hardness of the interface was dependent on the intermetallic phase of the interface.
- Fractography of the fatigue samples revealed that cracks nucleated at the interface, propagated along the interface, and continued through the substrate perpendicular to the surface.
- The cold-spray processing parameters influenced the microstructure of the Zn coating. At a low coating temperature, the microstructure of the coating comprised lamellar grains, creating an integrated dense coating. However, with an increase in the carrier gas temperature, undeformed particles were more likely to be trapped in the coating, thus creating defects such as porosity in the coating.
- The interaction between the impact-induced peening and thermal mismatch on the microstructure of AZ31B was shown to develop grain refinement near the interface and various grain structures further away in response to the coating conditions.
- Residual stress observations showed that compressive residual stress developed at the interface of the Zn coating and AZ31B substrate at the carrier gas temperature range used in this study. However, the increase of the gas temperature induced detrimental residual stress at the Zn coating surface owing to the thermal mismatch effect.
- Deposition of the Zn coating as an interlayer between the Al7075 coating and AZ31B Mg substrate resulted in the formation of compressive residual stress in all three layers.

CRediT authorship contribution statement

Bahareh Marzbanrad: Conceptualization, Methodology, Data curation, Formal analysis, Validation, Visualization, Writing – original draft. **Ehsan Toyserkani:** Conceptualization, Supervision, Methodology, Validation, Writing - review & editing. **Hamid Jahed:** Conceptualization, Methodology, Validation, Resources, Supervision, Funding acquisition, Writing – review & editing.

Declaration of competing interest

The authors declare that they have no known competing financial interests or personal relationships that could have appeared to influence the work reported in this paper.

Acknowledgments

Financial support through funds from Natural Sciences and Engineering Research Council of Canada (NSERC) RTI program under EQPEQ458441-2014 grant, and NSERC through APC under APCPJ 459269–13 grant are gratefully acknowledged.

References

[1] A. Papyrin, V. Kosarev, S. Klinkov, A. Alkhimov, V. Fomin, Cold Spray Technology, 1st ed., Elsivier, Amsterdam, 2006.
[2] H. Assadi, H. Kreye, F. Gärtner, T. Klassen, Cold spraying – a materials perspective, Acta Mater. 116 (2016) 382–407, https://doi.org/10.1016/j.actamat.2016.06.034.
[3] B. Marzbanrad, E. Toyserkani, H. Jahed, Customization of residual stress induced in cold spray printing, J. Mater. Process. Technol. 289 (2021), 116928, https://doi.org/10.1016/j.jmatprotec.2020.116928.
[4] B. Marzbanrad, M. Razmpoosh, E. Toyserkani, H. Jahed, Role of heat balance on the microstructure evolution of cold spray coated AZ31B with AA7075, J. Magnes. Alloy. Accepted (2021), https://doi.org/10.1016/j.jma.2021.03.009.
[5] T. Suhonen, T. Varis, S. Dosta, M. Torrell, J.M. Guilemany, Residual stress development in cold sprayed Al, cu and Ti coatings, Acta Mater. 61 (2013) 6329–6337, https://doi.org/10.1016/j.actamat.2013.06.033.
[6] R. Ghelichi, D. MacDonald, S. Bagherifard, H. Jahed, M. Guagliano, B. Jodoin, Microstructure and fatigue behavior of cold spray coated Al5052, Acta Mater. 60 (2012) 6555–6561. doi:https://doi.org/10.1016/j.actamat.2012.08.020.
[7] B. Marzbanrad, E. Toyserkani, H. Jahed, Multi-layer cold spray coating: strain distribution, Key Eng. Mater. 813 (2019) 411–416. doi:10.4028/www.scientific.net/KEM.813.411.
[8] B. Marzbanrad, H. Jahed, E. Toyserkani, On the evolution of substrate's residual stress during cold spray process: a parametric study, Mater. Des. 138 (2018) 90–102, https://doi.org/10.1016/j.matdes.2017.10.062.
[9] K. Ogawa, Cold spray coatings, 2017. doi:https://doi.org/10.3131/jvsj2.60.187.
[10] M. Krystýnová, P. Doležal, S. Fintová, M.M. Březina, J. Zapletal, J. Wasserbauer, Preparation and characterization of zinc materials prepared by powder metallurgy, Metals (Basel). 7 (2017) 396. doi:https://doi.org/10.3390/met7100396.
[11] G.K. Levy, J. Goldman, E. Aghion, The prospects of zinc as a structural material for biodegradable implants—a review paper, Metals (Basel). 7 (2017) 1–18, https://doi.org/10.3390/met7100402.
[12] N.M. Chavan, B. Kiran, A. Jyothirmayi, P.S. Phani, G. Sundararajan, The corrosion behavior of cold sprayed zinc coatings on mild steel substrate, J. Therm. Spray Technol. 22 (2013) 463–470, https://doi.org/10.1007/s11666-013-9893-z.
[13] C.-J. Li, W.-Y. Li, Y.-Y. Wang, Formation of metastable phases in cold-sprayed soft metallic deposit, Surf. Coatings Technol. 198 (2005) 469–473, https://doi.org/10.1016/j.surfcoat.2004.10.063.
[14] N.B. Maledi, O.P. Oladijo, I. Botef, T.P. Ntsoane, A. Madiseng, L. Moloisane, Influence of cold spray parameters on the microstructures and residual stress of Zn coatings sprayed on mild steel, Surf. Coatings Technol. 318 (2017) 106–113, https://doi.org/10.1016/j.surfcoat.2017.03.062.
[15] J.G. Legoux, E. Irissou, C. Moreau, Effect of substrate temperature on the formation mechanism of cold-sprayed aluminum, zinc and tin coatings, J. Therm. Spray Technol. 16 (2007) 619–626, https://doi.org/10.1007/s11666-007-9091-y.
[16] B. Marzbanrad, The Effect of Cold Spray Coating Parameters on the Residual Stress and Fatigue Performance of Magnesium Alloys, University of Waterloo, 2019.
[17] Metal Handbook: 4E: Heat Treating of Nonferrous Alloys, ASM International, 2018.
[18] H. Assadi, T. Schmidt, H. Richter, J.O. Kliemann, K. Binder, F. Gärtner, T. Klassen, H. Kreye, On parameter selection in cold spraying, J. Therm. Spray Technol. 20 (2011) 1161–1176, https://doi.org/10.1007/s11666-011-9662-9.
[19] J. Pattison, S. Celotto, A. Khan, W. O'Neill, Standoff distance and bow shock phenomena in the cold spray process, Surf. Coatings Technol. 202 (2008) 1443–1454, https://doi.org/10.1016/j.surfcoat.2007.06.065.
[20] G. Mauer, R. Singh, K.H. Rauwald, S. Schrüfer, S. Wilson, R. Vaßen, Diagnostics of cold-sprayed particle velocities approaching critical deposition conditions, J. Therm. Spray Technol. 26 (2017) 1423–1433. doi:https://doi.org/10.1007/s11666-017-0596-8.
[21] A.W.-Y.Y. Tan, W. Sun, A. Bhowmik, J.Y. Lek, I. Marinescu, F. Li, N.W. Khun, Z. Dong, E. Liu, Effect of coating thickness on microstructure, mechanical properties and fracture behaviour of cold sprayed Ti6Al4V coatings on Ti6Al4V substrates, Surf. Coatings Technol. 349 (2018) 303–317, https://doi.org/10.1016/j.surfcoat.2018.05.060.
[22] A. Viscusi, A. Astarita, R. Della Gatta, F. Rubino, A perspective review on the bonding mechanisms in cold gas dynamic spray, Surf. Eng. 35 (2019) 743–771, https://doi.org/10.1080/02670844.2018.1551768.
[23] K.H. Ko, J.O. Choi, H. Lee, Intermixing and interfacial morphology of cold-sprayed Al coating on steel, Mater. Lett. 136 (2014) 45–47, https://doi.org/10.1016/j.matlet.2014.07.142.
[24] K.H. Ko, J.O. Choi, H. Lee, Y.K. Seo, S.P. Jung, S.S. Yu, Cold spray induced amorphization at the interface between Fe coating Al substrate, Mater. Lett. 149 (2015) 40–42, https://doi.org/10.1016/j.matlet.2015.02.118.
[25] S. Guetta, M.H.H. Berger, F. Borit, V. Guipont, M. Jeandin, M. Boustie, Y. Ichikawa, K. Ogawa, K. Sakaguchi, K. Ogawa, Influence of particle velocity on adhesion of cold-sprayed splats, J. Therm. Spray Technol. 18 (2009) 331–342, https://doi.org/10.1007/s11666-009-9327-0.
[26] H. Lee, H. Shin, K. Ko, Effects of gas pressure of cold spray on the formation of Al-based intermetallic compound, J. Therm. Spray Technol. 19 (2010) 102–109, https://doi.org/10.1007/s11666-009-9407-1.
[27] S. Barradas, V. Guipont, R. Molins, M. Jeandin, M. Arrigoni, M. Boustie, C. Bolis, L. Berthe, M. Ducos, Laser shock flier impact simulation of particle-substrate interactions in cold spray, J. Therm. Spray Technol. 16 (2007) 548–556, https://doi.org/10.1007/s11666-007-9069-9.
[28] Helmut Mehrer, Diffusion in Solids, Springer, Berlin, 2007, https://doi.org/10.1007/987-3-319-48206-4.
[29] D. Zhang, P.H. Shipway, D.G. McCartney, Cold gas dynamic spraying of aluminum: the role of substrate characteristics in deposit formation, J. Therm. Spray Technol. 14 (2005) 109–116, https://doi.org/10.1361/10599630522666.
[30] A. Wank, B. Wielage, H. Podlesak, T. Grund, High-resolution microstructural investigations of interfaces between light metal alloy substrates and cold gas-sprayed coatings, J. Therm. Spray Technol. 15 (2006) 280–283, https://doi.org/10.1361/105996306X108291.
[31] W.Y. Li, C. Zhang, X. Guo, C.J. Li, H. Liao, C. Coddet, Study on impact fusion at particle interfaces and its effect on coating microstructure in cold spraying, Appl. Surf. Sci. 254 (2007) 517–526, https://doi.org/10.1016/j.apsusc.2007.06.026.
[32] P.C. King, G. Bae, S.H. Zahiri, M. Jahedi, C. Lee, An experimental and finite element study of cold spray copper impact onto two aluminum substrates, J. Therm. Spray Technol. 19 (2010) 620–634, https://doi.org/10.1007/s11666-009-9454-7.
[33] P.C. King, S.H. Zahiri, M. Jahedi, Focused ion beam micro-dissection of cold-sprayed particles, Acta Mater. 56 (2008) 5617–5626, https://doi.org/10.1016/j.actamat.2008.07.034.
[34] X.J. Ning, J.H. Jang, H.J. Kim, C.J. Li, Changhee Lee, Cold spraying of Al-Sn binary alloy: coating characteristics and particle bonding features, Surf. Coatings Technol. 202 (2008) 1681–1687, https://doi.org/10.1016/j.surfcoat.2007.07.026.
[35] A.V. Bolesta, V.M. Fomin, M.R. Sharafutdinov, B.P. Tolochko, Investigation of interface boundary occurring during cold gas-dynamic spraying of metallic particles, Nucl, Instruments Methods Phys. Res. Sect. A Accel. Spectrometers, Detect. Assoc. Equip. 470 (2001) 249–252, https://doi.org/10.1016/S0168-9002(01)01067-1.
[36] S.K. Shaha, H. Jahed, An in-situ study of the interface microstructure of solid-state additive deposition of AA7075 on AZ31B substrate, Appl. Surf. Sci. 508 (2020), 144974, https://doi.org/10.1016/j.apsusc.2019.144974.
[37] W.Y. Li, C.J. Li, G.J. Yang, Effect of impact-induced melting on interface microstructure and bonding of cold-sprayed zinc coating, Appl. Surf. Sci. 257 (2010) 1516–1523, https://doi.org/10.1016/j.apsusc.2010.08.089.
[38] R. Ninomiya, H. Yukawa, M. Morinaga, K. Kubota, An electronic approach to the prediction of the mechanical properties of magnesium alloys, J. Alloys Compd. 215 (1994) 315–323, https://doi.org/10.1016/0925-8388(94)90860-5.
[39] C.C. Kammerer, S. Behdad, L. Zhou, F. Betancor, M. Gonzalez, B. Boesl, Y.H. Sohn, Diffusion kinetics, mechanical properties, and crystallographic characterization of intermetallic compounds in the Mg-Zn binary system, Intermetallics. 67 (2015) 145–155, https://doi.org/10.1016/j.intermet.2015.08.001.
[40] V.K. Champagne, D.J. Helfritch, M.D. Trexler, B.M. Gabriel, The effect of cold spray impact velocity on deposit hardness, model, Simul. Mater. Sci. Eng. 18 (2010) 65011, https://doi.org/10.1088/0965-0393/18/6/065011.
[41] D.R. Askeland, P.P. Fulay, W.J. Wright, The Science and Engineering of Materials, 6th ed., Cengage Learning, Stamford, USA, 2011.
[42] J. Watanabe, Fatigue properties of zinc single crystals and polycrystals, I, Fatigue Strength, Trans. Japan Inst. Met. 3 (1962) 14–20, https://doi.org/10.2320/matertrans1960.3.14.
[43] S. Morita, N. Ohno, F. Tamai, Y. Kawakami, Fatigue properties of rolled AZ31B magnesium alloy plate, Trans. Nonferrous Met. Soc. China. 20 (2010) S523–S526, https://doi.org/10.1016/S1003-6326(10)60531-6.